Journal of Structural Geology 33 (2011) 1541–1553

Contents lists available at SciVerse ScienceDirect

Journal of Structural Geology

journal homepage: www.elsevier.com/locate/jsg

In-situ characterization of the effective elasticity of a fault zone, and its relationship to fracture spacing

Philippe Steer[a,b,*], Aurélien Bigot[a], Rodolphe Cattin[a], Roger Soliva[a]

[a] Géosciences Montpellier, CNRS-UMR 5243, Université Montpellier 2, 34000 Montpellier, France
[b] Laboratoire de Géologie, CNRS-UMR 8538, Ecole Normale Supérieure, 75005 Paris, France

ARTICLE INFO

Article history:
Received 20 October 2010
Received in revised form
2 September 2011
Accepted 12 September 2011
Available online 17 September 2011

Keywords:
Fault zone
Fracture spacing
Fracture stiffness
Effective elasticity
Schmidt hammer
Fracture healing

ABSTRACT

In this paper, we describe an outcrop to characterize the effect of fracture spacing and type on larger scale effective elasticity, which is measured for the first time in-situ with a Schmidt hammer. The outcrop is dominated by lime mudstones and belongs to the deformation zone of the St Clément fault, in southern France. Our results suggest that small spacing of faults, open fractures and styolites leads to lesser effective Young's modulus, whereas small sealed fracture spacing leads to greater effective Young's modulus. These relationships are compatible with theoretical models of effective elasticity. Using Amadei and Savage (1993) approach, we define a non-linear model that relates Schmidt hammer rebound to spacing by fracture type. A hemisphere with a radius of 40 to ~200 cm is the rheological volume characterized by the Schmidt hammer. Results of model inversion demonstrate that variations of Schmidt hammer rebound over the outcrop can be used to estimate fracture type and stiffness. Stiffness of sealed fractures is 2–3 orders of magnitude greater than the stiffness of faults, stylolites and open fractures. This result is consistent with an increase of the rate of interseismic stress build-up of major faults with sealing of fractures in their damage zone.

1. Introduction

Rocks discontinuities, such as faults or fractures, play a major role in geological systems, leading to heterogeneity and anisotropy in hydraulic, thermal as well as geomechanical properties of rocks. The spatial density or spacing of mechanical discontinuities significantly affects the elastic behavior of a fractured rock medium (Bristow, 1960; Walsh, 1965; O'Connell and Budiansky, 1974; Kachanov, 1980; Hudson, 1980; Schoenberg, 1980; Amadei and Savage, 1993; Bieniawski, 1993), its compressive strength (Kemeny and Cook, 1992), its permeability to fluids (Renshaw, 1996), the brittle strain of a fault population (Scholz and Cowie, 1990; Schultz, 2003) and the bedrock resistance to river or glacier erosion (Molnar et al., 2007). For instance, the architecture of major upper crustal fault zones is commonly represented by a central zone of protocataclasite and ultracataclasite, surrounded by a large damage or process zone containing micro and macro-fractures (*e.g.*, Caine et al., 1996). These fractures affect the mechanical effective properties of the damage zone and thus the behavior and growth of major faults zone (Segall and Pollard, 1980; Cowie and Scholz, 1992; Katz et al., 2000; Aydin, 2009) and their slip distributions (Bürgmann et al., 1994).

A common way to characterize the mechanical effects of fractures on a rock mass, consists of assessing the resulting effective properties from both laboratory experiments (*e.g.*, Sayers & Kachanov, 1995) and theoretical approaches (*e.g.*, Hudson, 1980; Kachanov, 1992; Amadei and Savage, 1993). Because of potential scale effects associated with mechanical discontinuities (*e.g.*, Schlische at al., 1996; Bonnet et al., 2001), the upscaling of the effective rock properties determined from laboratory samples or other small scale measurements (<0.1 m) to the scale of a fault zone (>1 m) is a major issue (*e.g.*, Guéguen et al., 2006).

In-situ experiments offer a way to apply mechanical models at a much larger scale. For instance, the stiffness of fractures with a characteristic length of 1–10 m can be constrained using field seismic experiments (Lubbe and Worthington, 2006; Worthington and Lubbe, 2007) or by combining numerical mechanical model with detailed fracture geometries (Griffith et al., 2009). At a larger scale, the mechanical properties of majors fault zones (10^2–10^3 m) can be inferred from the study of seismic trapped waves (Ben-Zion et al., 2003) or by modeling of geodesic data (Fialko, 2004).

* Corresponding author. Department of Earth Sciences, Bergen University, Allegaten 41, N-5007 Bergen, Norway . Tel.: +47 55 58 35 41.
E-mail addresses: philippe.steer@gmail.com, philippe.steer@gm.univ-montp2.fr (P. Steer), aurelien.bigot@hotmail.fr (A. Bigot), cattin@gm.univ-montp2.fr (R. Cattin), soliva@gm.univ-montp2.fr (R. Soliva).

0191-8141/$ – see front matter © 2011 Elsevier Ltd. All rights reserved.
doi:10.1016/j.jsg.2011.09.009

At an intermediate scale (0.1–1 m) between laboratory and these larger scale in-situ experiments, the Schmidt hammer allows one to obtain a direct and in-situ estimate of the conducted hardness. In particular, its measurements are found to correlate with the Young's modulus of a rock mass (*e.g.*, Deere and Miller, 1966; Aydin and Basu, 2005; Goudie, 2006).

In this paper, we investigate the effect of fracture types and spacing on the effective elasticity of a fault zone. Effective elasticity is estimated with a high density of Schmidt hammer measurements (25 measurements per square meters). This analysis is applied to an outcrop located close to the St Clément fault zone, in southern France. Qualitative as well as mechanical analysis of rock effective elasticity in relation to fracture properties are conducted. The robustness and validity of a proposed rheological model, derived from theoretical and empirical predictions, is discussed with respect to the measurements.

2. Data and qualitative results

The study area is located close to the St Clément fault zone (~10 km North of Montpellier, France, Fig. 1), where fracture development is already well documented (Taha, 1986; Soliva et al., 2010) and is similar to other related faults (Etchecopar et al., 1981; Rispoli, 1981). Data were collected along an outcrop (19 m × 3 m) oriented perpendicular to the major fault within the study area. The dataset includes both a detailed mapping of fractures and a dense set of Schmidt hammer measurements (Fig. 2).

2.1. Study outcrop: St Clément fault zone

In the study area, many faults appear to be limited at depth by a Triassic weak mechanical layer (evaporitic level) allowing a major décollement in which the St Clément fault probably terminates into (Benedicto, 1996; Séranne et al., 1995). The St Clément fault therefore cuts the Post-Triassic sediment cover with close to 500 m of cumulated displacement in the study area. At the surface, the fault cuts the Lower Cretaceous series composed of lime mudstones, marly mudstones and marls from the Berriasian marine inner platform environment (Fig. 1). The outcrop exposes the footwall of the eroded main fault zone and exhibits mainly decimetric to metric lime mudstones layers interbeded with thin (centimetric) marl layers (Fig. 2A). Layers have constant thickness and laterally, lithologies are continuous at the scale of the outcrop. Marls are mainly observed in the outcrop within a secondary fault core of this fault zone. These marls are a structural product of smearing of a thick marl layer that is stratigraphically present at tens of meters above the footwall exposure in the outcrop as part of the upper Berriasian series. The fault zone exhibits multiple sets of fractures and stylolites which have been related to different tectonic events of this region (Etchecopar et al., 1981; Taha, 1986).

Regional tectonic relationships suggest that St Clément fault had a three-phase tectonic history: (1) a normal dip-slip phase during an NW-SE middle Cretaceous extension; (2) a sinistral strike-slip phase during the Paleocene-Eocene Pyrenean compression; and (3) a main normal dip-slip phase during the Oligocene-Aquitanian NW-SE rifting of the Gulf Lion (Arthaud and Mattauer, 1969). The brittle structures observed on the outcrop (Fig. 2 A, B) were mainly formed during this third phase of extension (Auzende et al., 1973; Séranne et al., 1995; Benedicto, 1996). The main surface of the studied fault, which has a 60° dip, also shows sinistral strike-slip components related to the second phase. Therefore, even if a minor part of the deformation may be related to strike-slip faulting, most of the fractures, the stylolites, the cataclastic fault core and the fault surfaces are consistent with normal faulting.

2.2. Brittle deformation and mapping

The outcrop presents two secondary faults to the main St Clément fault that each have tens of meters of normal displacement. The North-West fault exhibits a cataclastic core while the South-East fault has a shale-smeared core (Fig. 2A). These two faults are surrounded by their kinematically coherent damage zones composed of minor normal faults, mode I fractures sealed by sparite (i.e. a coarse crystalline calcite cement), bed parallel stylolites and also unsealed open fractures around the top of the outcrop that are randomly oriented and could possibly be related to Pliocene to Quaternary freezing and thawing cycles. To assess spatial distribution, these different types of fractures were mapped (Fig. 2B). Only fractures with a minimum tracelength of ~5 cm were mapped. A coordinate mesh composed of squares with dimension of 1 m × 1 m is used to offer a common spatial referential with the Schmidt hammer dataset.

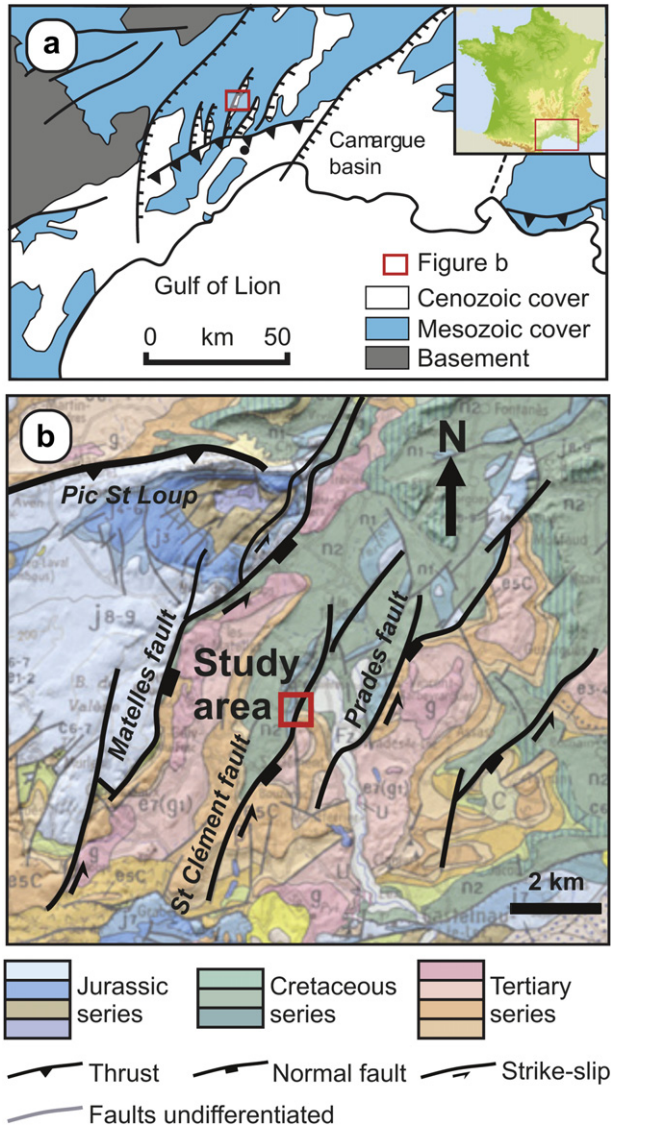

Fig. 1. (a) Geological and tectonic setting of southern France. Red box shows the location of subsequent figure. Inset shows location of study area (box) relative to France. (b) Simplified geological map of area. Heavy black lines show the major faults. The red box precises the location of the studied area. (For interpretation of the references to colour in this figure legend, the reader is referred to the web version of this article.)

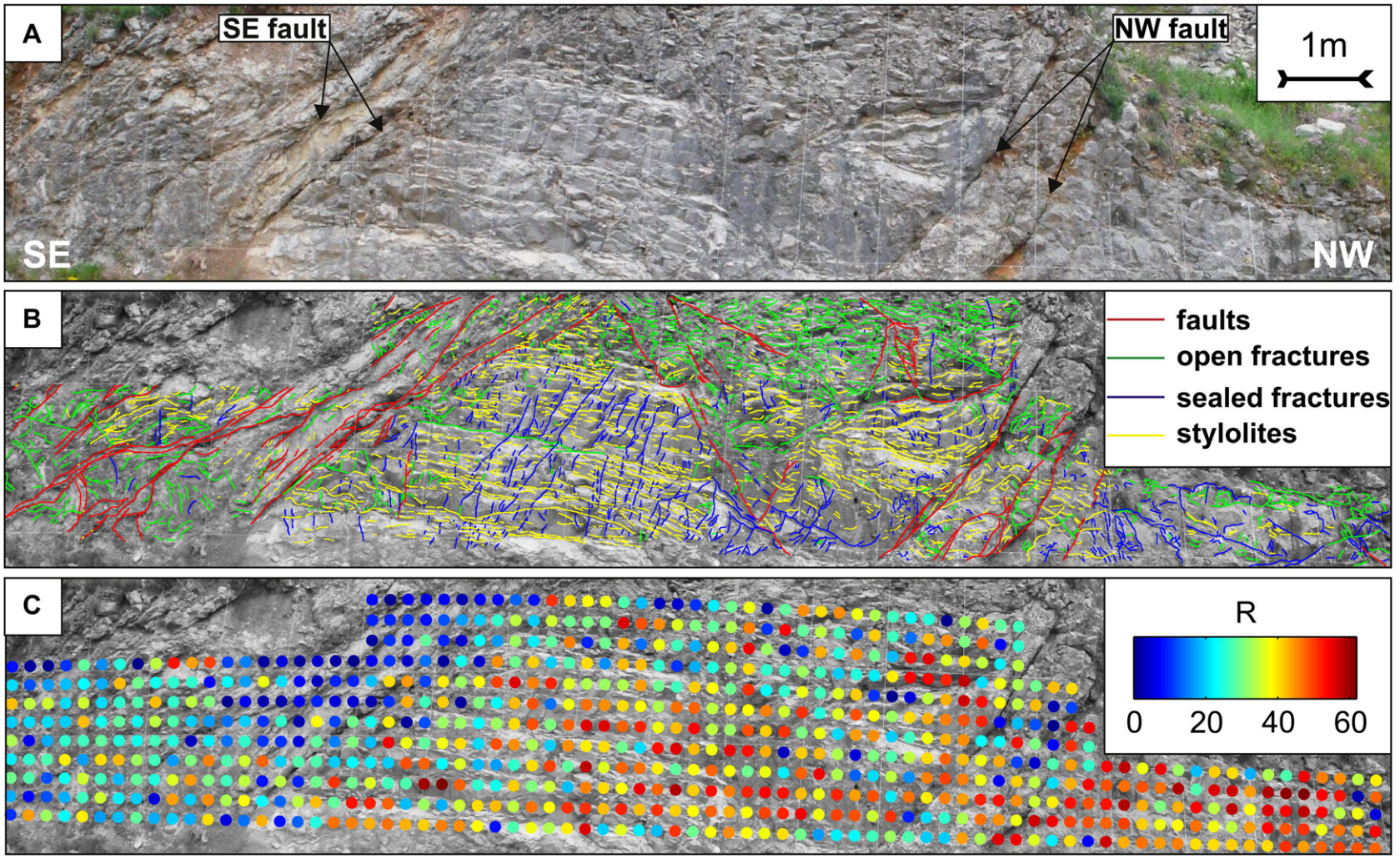

Fig. 2. (A) In terms of lithology the studied outcrop mostly consists of gray lime mudstone with parts of brown marlstone and cataclasites located within the SE and NW secondary fault zones, respectively. (B) Four types of fractures are considered : faults (red lines), open fractures (green lines), sealed fractures (blue lines) and stylolites (yellow lines). (C) Spatial distribution of Schmidt hammer rebound. (For interpretation of the references to colour in this figure legend, the reader is referred to the web version of this article.)

2.3. Schmidt hammer rebound

The Schmidt hammer consists of a spring-loaded mass that is released against a plunger when the hammer is pressed onto a hard surface. Part of the impact energy is consumed by absorption, *i.e.* plastic deformation under the plunger tip, and by transformation into heat and sound. The remaining energy represents the impact penetration resistance (or hardness) which induces the rebound of the mass (Basu and Aydin, 2004). The distance traveled by the mass after the rebound, expressed as a percentage of its initial distance to the plunger, is called the rebound (R hereinafter, see Table 1 for the definition of the variables used in this paper). To a first order, the Schmidt hammer hardness correlates with the uniaxial compressive strength (UCS) and Young's modulus (E) of materials (see Deere and Miller (1966), Aydin and Basu (2005) or Yagiz (2009) for a review). However, it is also sensitive to other properties such as surface smoothness, rock density, cementation, weathering and moisture content (*e.g.*, McCarroll, 1991; Sumner and Nel, 2002; Goudie, 2006).

Measurements are performed using the standard (N-type) Proceq Schmidt hammer that releases an impact energy of 2.207 N.m. Rebound is corrected from the influence of gravitational forces using the automatic normalization provided by the manufacturer. Each rebound value R is obtained from a total of ten consecutive, mostly horizontal impacts. The rebound value increases between the first and the second impact, while the subsequent impacts only produce minor changes (Fig. 3). This rebound increase can be associated with the weathering grade of the outcrop and the change in subsequent rebounds can be related to minor collapse or cracking beyond the original zone of compaction (Aydin and Basu, 2005). Consequently, we use the mean rebound value, R_{mean}, of the last eight impacts at each site ($R = R_{mean}$) to avoid the influence of surface weathering on characterizing material properties. In this study, the Schmidt hammer was found to be empirically sensitive to R ranging from 15 to 62. Rebounds less than 15 were not measured by the Schmidt hammer. However, these unmeasured rebounds ($0 < R < 15$), which are related to lesser rock hardness, need to be accounted for. Thus, for the sake of simplicity, we arbitrarily decided to randomly distribute these values between 0 and 15.

To evaluate the material heterogeneity of the outcrop, we use a closely spaced grid pattern of measurement points (Fig. 2C). A spacing of 25 cm between each Schmidt hammer measurement is used, yielding 739 rebound values from 7390 impacts.

Table 1
Table of variables.

Variable	Definition
A	Area of the sliding window
a	First parameter of the relationship between E and R
b	Second parameter of the relationship between E and R
E	Young's modulus
E_{eff}	Effective Young's modulus
E_0	Intact rock Young's modulus
k	Apparent fracture stiffness
k_i	Apparent fracture stiffness of the i -th fracture set
$k^{(n)}$	Normal fracture stiffness
$k^{(s)}$	Shear fracture stiffness
l	Fracture length
L_{window}	Radius of the sliding window
N	Number of fracture sets
R	Schmidt hammer rebound
R_0	Intact rock Schmidt hammer rebound
R_{blur}	Blurred Schmidt hammer rebound
R_{model}	Modeled Schmidt hammer rebound
$R_{model-all}$	Modeled Schmidt hammer rebound over the entire outcrop
S	Fracture spacing
S_i	Fracture spacing of the i -th fracture set
θ	Fracture inclination angle

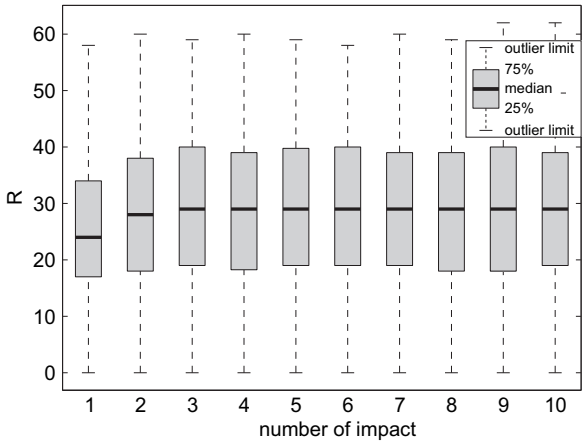

Fig. 3. Whisker plot showing the variation of R as a function of the number of impacts, for the entire dataset (739 measurements).

2.4. Distribution of fractures and Schmidt hammer rebound

To evaluate a preliminary spatial distribution between fracture occurence and R values, we compute the distribution of R with respect to each fracture type. Each Schmidt hammer measurement site may intersect several fracture types (Fig. 2). Therefore, the presence of each fracture type was recorded where a fracture at a distance less than 20 cm from a measurement center was present and was included as an abundance count (Fig. 4). This radius of 20 cm was chosen to be just below the distance between successive Schmidt hammer measurement 25 cm, thereby limiting the redundancy of fractures into the distribution, and sufficiently large to document the fractures that may affect the measure.

The resulting distributions show three different relationships between fracture types and R : (1) faults are less well represented for large values of R (>20) (Fig. 4A); (2) sealed fractures are less well represented for small values of R (Fig. 4C); and (3) open fractures and stylolites are equally-well represented for each value or R because they occur at almost all measurement sites (Figs. 2 and 4). Thus, contrary to faults and sealed fractures, open fractures and stylolites are not expected to have a significant statistical effect on R. In the following, we mechanically analyze the relationships between R and the spatial distribution of fracture type to further investigate these results.

3. Mechanical analysis and modeling

3.1. Effective elastic medium

Compared to intact rocks, fractured rock masses show increased deformability. Three main approaches account for the effect of fractures on rock mass elasticity: (1) empirically reducing the effective elastic modulus deduced from laboratory measurements of intact rock samples (*e.g.*, Bieniawski, 1978); (2) considering each fracture as an individual discrete feature embedded into a continuous ideal elastic continuum (*e.g.*, Mahtab, 1969; Belytschko et al., 1984; Griffith et al., 2009); and (3) defining an effective elastic continuum that accounts for the orientation, spatial distribution and stiffness of fractures (*e.g.*, Hudson, 1980; Kachanov, 1992; Amadei and Savage, 1993).

In this third approach, different sets of fractures that share the same stiffness and orientation can be treated simultaneously (Hudson, 1981). Given the spatial correlation of Schmidt hammer

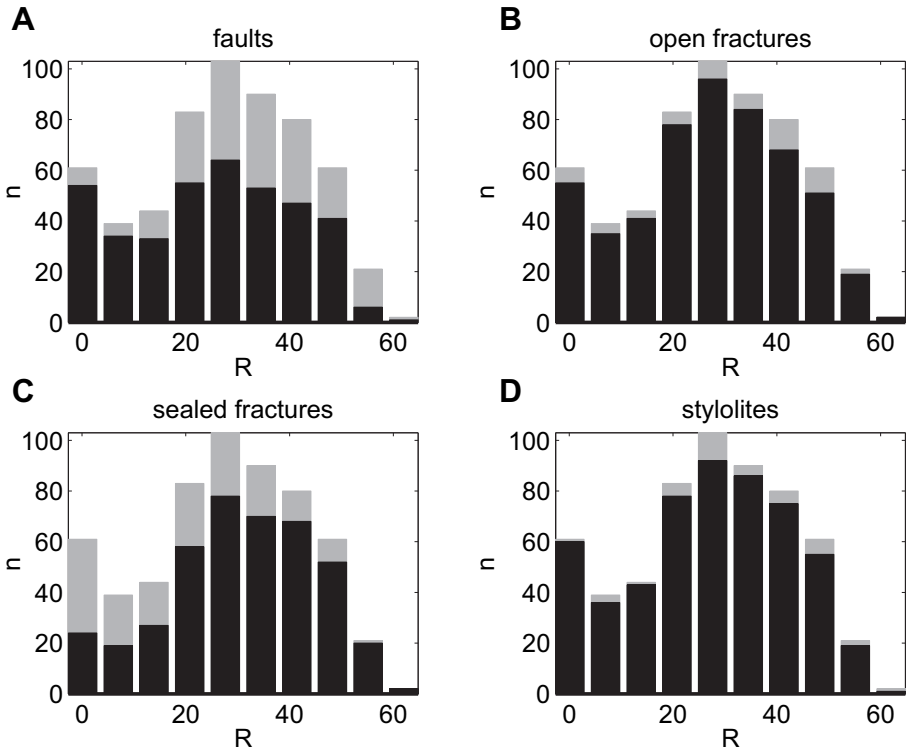

Fig. 4. Schmidt hammer histogram distribution (10 bins) associated with each type of fracture (black bars): (A) faults, (B) open fractures, (C) sealed fractures, and (D) stylolites. The gray bars give the total distribution related to all fractures. *n* is the number (or count) of Schmidt hammer measurements. Note that the total sum of the distributions obtained in this way, is not equal to the total distribution related to all fractures.

rebound to fracture type in the outcrop (Fig. 4), we have the opportunity to use this third approach to yield a description of the elastic properties of this domain at the scale of a few centimeters to a few meters, accounting for the actual discontinuities in the rock.

Two formulations of effective elastic medium are classically defined, which mainly differ by their assumption concerning the relative dimension of the discontinuities and medium considered: 1) the characteristic dimension of discontinuities is small compared to the size of the medium (*e.g.*, Walsh, 1965; Hudson, 1980; Kachanov, 1992; Grechka & Kachanov, 2006); or 2) the characteristic dimension of discontinuities is similar or greater than the size of the medium (*e.g.*, Duncan and Goodman, 1968; Amadei and Savage, 1993). With respect to the settings of our experiment, the first formulation is valid if the characteristic dimension of fractures is small compared to the wavelength of the elastic waves dynamically generated during a Schmidt hammer impact. To our knowledge, no constraint exists concerning these wavelengths in limestones nor any other rock type. However, Rotonda (2001) found that Schmidt hammer impact generates body and surface waves with a velocity around 2 km^{-1} for Rayleigh waves and 3 km s^{-1} for P waves in concretes. The frequencies of both have a broad spectrum, and the maximum recorded frequency is 45 kHz (Rotonda, 2001). These velocities and this frequency provide an estimate of the lower bound for the wavelength of the waves generated by a Schmidt hammer impact at 4.5 cm and 6.5 cm for Rayleigh and P waves, respectively. These wavelengths are about the same order of magnitude than the median tracelength of open fractures, 12 cm, sealed fractures, 10 cm, stylolites, 9 cm, and faults, 42 cm (Fig. 5). This rules out the possibility of using such effective elastic medium formulation (*e.g.*, Walsh, 1965; Hudson, 1980; Kachanov, 1992).

In contrast, the effective medium theory developed by Duncan and Goodman (1968) and then Amadei and Savage (1993) is more adapted, because the wavelength of the waves generated by a Schmidt hammer impact corresponds to the characteristic dimension of the fractures of our study. Its main assumptions are (1) that the fractures of each fracture set are regularly spaced and share the same orientation and stiffness, which is reasonable when considering our study, because the fractures of each fracture set

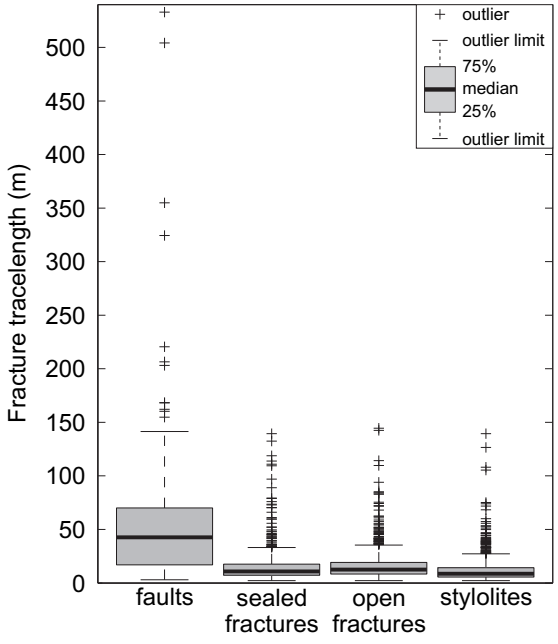

Fig. 5. Whisker plot showing the distribution over the entire outcrop of tracelength for the different fracture sets.

share a common history, therefore they are mostly parallel (Fig. 2B) and we can assume their stiffness to be roughly identical; (2) that the intact rock is linearly elastic, which is respected for incremental changes in stress (*e.g.*, Jaeger et al., 2007); and (3) that the medium considered is large enough to contain numerous fractures, yet small enough to make strain and stress gradients negligible within it. The validity of this last assumption is clearly dependent on the scale investigated to compare Schmidt hammer rebound and fracture distribution.

3.2. Elastic properties of mesoscopic fractures

Following this last approach, fracture spacing, normal and shear stiffness with respect to rock mass deformability, may be accounted for (Duncan and Goodman, 1968; Amadei and Savage, 1993). Let us consider a rock mass under uniaxial loading in the *Y* direction, normal to the *X Z* plane, *i.e.* the surface of the outcrop (Fig. 6). This rock mass is cut by a parallel and regular fracture set that is inclined with an angle θ from the *X Z* plane. This fracture set has a spacing *S*, and each fracture has the same normal and shear stiffness $k^{(n)}$ and $k^{(s)}$, respectively. In this setting, the effective Young's modulus E_{eff} relating stress and strain in the *Y* direction is given by,

$$\frac{1}{E_{eff}} = \frac{1}{E_0} + \frac{\cos^4\theta}{k^{(n)}S} + \frac{\sin^2 2\theta}{4k^{(s)}S}, \tag{1}$$

with E_0 the intact rock Young's modulus.

Applying this model to the outcrop requires considerations of the limitations of the available dataset: (1) the orientation of the faults and fractures with respect to the outcrop surface is poorly constrained, because we lack information about their three-dimensional geometry. As a consequence, it is impossible to distinguish the respective contribution of normal and shear fracture deformability to the effective Young's modulus. Given this problem, an apparent stiffness *k* can be defined that encompasses fracture inclination, normal and shear stiffness, $k_i = 1/(\cos^4\theta/k^{(n)} + \sin^2 2\theta/4\cdot k^{(s)})$. (2) These four fracture sets, which are very likely to exhibit different stiffnesses and orientation, have to be taken into account independently of each other. In this context, we assume that the overall contribution to deformability of all fracture sets is equal to the sum of the contribution to deformability of each fracture set. Given that assumption, Equation (1) becomes,

$$\frac{1}{E_{eff}} = \frac{1}{E_0} + \sum_{i=1}^{N} \frac{1}{k_i \cdot S_i}, \tag{2}$$

with *N* as the number of fracture sets where $N = 4$, k_i the apparent stiffness of the *i* -th fracture set and S_i its spacing.

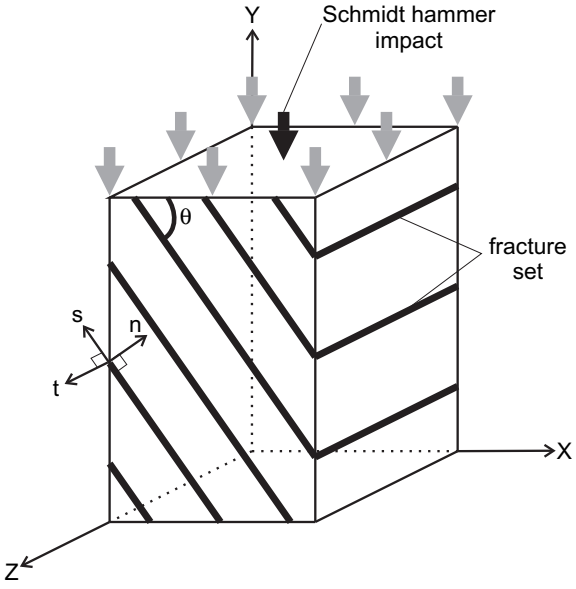

Fig. 6. Fractured rock under uniaxial loading. The black arrow indicates the point load by a Schmidt hammer, while the gray arrows indicate a classical uniaxial load. A regular fracture set with its angle inclination θ is indicated with solid bold lines.

3.3. Young's modulus and Schmidt hammer rebound

We wish to evaluate the effective Young's modulus of the fractured rock mass. Outcomes from empirical studies (see Aydin and Basu (2005), Goudie (2006), or Yagiz (2009) for a review) support either a linear (*e.g.*, Sachpazis, 1990; Dearman et al., 1978; Yagiz, 2009), a power-law (*e.g.*, Katz et al., 2000; Yagiz, 2009), or an exponential (*e.g.*, Xu et al., 1990; Yilmaz and Sendir, 2002; Aydin and Basu, 2005) relationship between *R* and the effective Young's modulus E_{eff},

$$E_{eff} = a \cdot R + b, \tag{3}$$

$$\text{or} \quad E_{eff} = b \cdot R^a, \tag{4}$$

$$\text{or} \quad E_{eff} = b \cdot \exp(a \cdot R), \tag{5}$$

with *a* and *b* as two constants that depend mainly on the lithology considered. We chose to use the linear elastic model because it is particularly adapted to carbonates (Sachpazis, 1990). Given that decision, substituing Equation (3) into Equation (2) leads to the following equation,

$$\frac{1}{a \cdot R + b} = \frac{1}{a \cdot R_0 + b} + \sum_{i=1}^{N} \frac{1}{k_i \cdot S_i}, \tag{6}$$

where R_0 is the Schmidt hammer rebound of the intact rock.

3.4. Fracture spacing

Fracture spacing is often measured using the 1*D line* or *scanline* method, where spacing is an average of the population of distances between adjacent fractures of the same set along the sampling line that ideally should be normal to mean fracture orientation for the set. However this approach yields a single value for spacing that does not characterize the heterogeneity of fracture spacing across an area or in a volume. While it is possible to measure a number of scanlines, a number of workers have shown that for an area, characterizing spacing by position is more easily achieved. We, therefore, use the approach of Wu and Pollard (1995) to spatially characterize the spacing distribution by fracture set on the outcrop surface. Practically we use a circular window to determine fracture spacing *S* (Fig. 7A–D),

$$S = \frac{A}{\pi \cdot L_{window} + \sum_{i=1}^{N} l_i^2}, \tag{7}$$

where *N* is the number of fractures intersecting the circular window of radius L_{window}, l_i the inscribed length of the *i* -th fracture inside the circular window, and $A(= \pi L_{window}^2)$ the area of the circular window. In a first time, we *apriori* set the radius L_{window} equal to 50 cm, which is equivalent to assume that the Schmidt hammer is sensitive to rock mass properties for a hemispherical volume with the same radius.

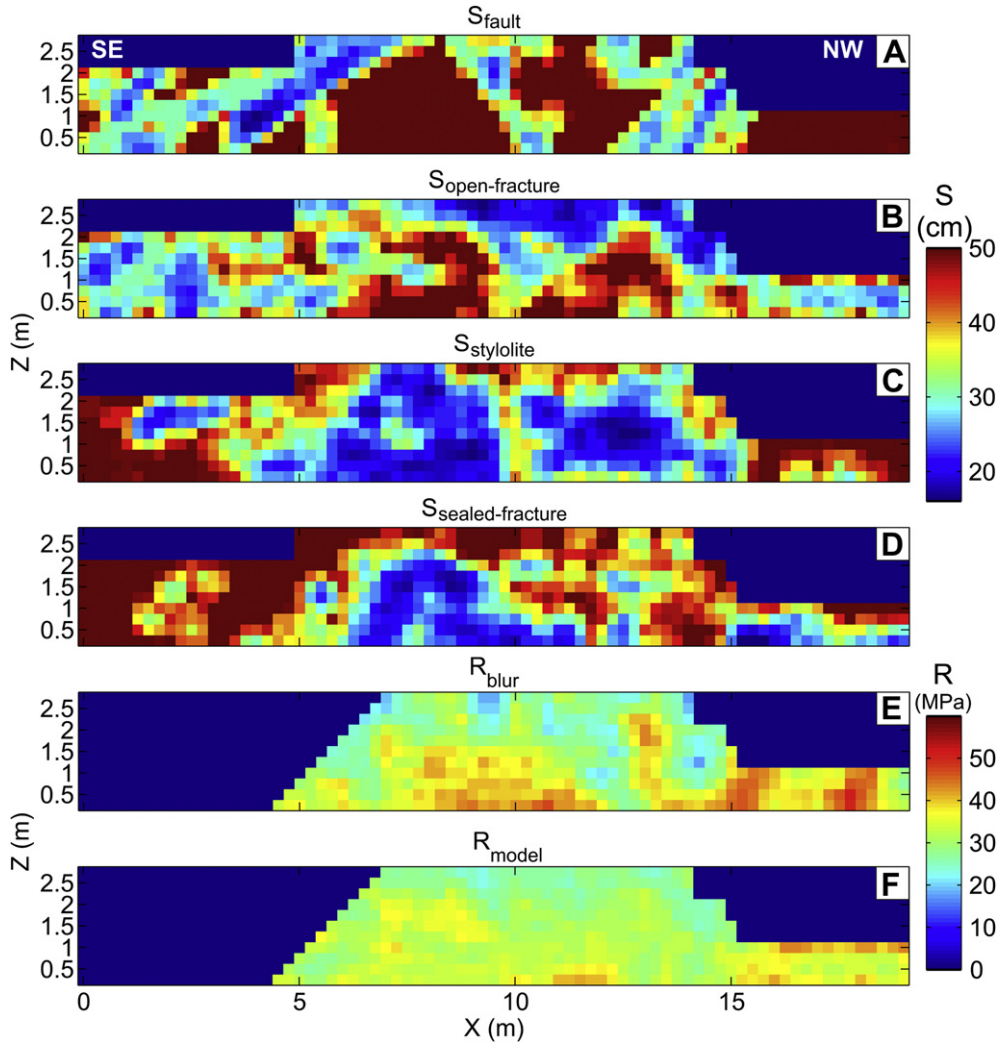

Fig. 7. Fracture spacing for each fracture type obtained with a circular sliding windows with a radius L_{window} = 50 cm : (A) fault, (B) open fracture, (C) stylolite and (D) sealed fracture. (E) Observed R_{blur} and (F) inverted R_{model} Schmidt hammer rebound distribution along the study outcrop, computed by only considering the lime mudstone parts of the outcrop.

3.5. Smoothing R

To further compare fracture spatial distribution and Schmidt hammer rebound values, we assume that a small but significant part of the spatial variations of R is not related to the distribution of mapped fractures (Fig. 2). This assumption is justified because: (1) fractures with a tracelength of less than 5 cm are not mapped, and these microfractures would contribute to the R value; (2) local variations of outcrop surface roughness, weathering grade and moisture content in the rock mass affect R (Aydin and Basu, 2005; McCarroll, 1991; Sumner and Nel, 2002); and (3) R may be undersampled because 10 is the lower bound of the range of 10–40 impacts needed at each site of measurement to statistically evaluate the rebound value R for limestones (Niedzielski et al., 2009). Thus, to minimize these local effects which are likely to induce some high spatial variability of R, we smooth (or blur) the values of R, using an averaging method taking into account the direct neighbours of each R value. Henceforth, only smoothed values of R will be considered (Fig. 7E vs Fig. 2C).

3.6. Model inversion

Equation (6) provides a theoretical framework to compare R and fracture spacing for the outcrop. This non-linear equation involves several unknown parameters: four apparent stiffnesses k_i, the intact rock rebound R_0, and the a and b parameters that define the relationship between R and E_{eff}. We constrain these unknown parameters by comparing the Schmidt hammer rebound obtained in-situ R_{blur} (*i.e.* the modified dataset) with the modeled rebound R_{model}, applying the values derived from the maps for fracture spacing to Equation (6). Determining the sets of parameters that yields the spatial distribution of R_{model} that best matches R_{blur} is achieved by minimizing the misfit function Φ, which is the difference between the modified data and the modeled rebound in a least-square sense,

$$\phi = \sum_m \sum_n \left(\frac{1}{a \cdot R_{blur}(m,n) + b} - \frac{1}{a \cdot R_{model}(m,n) + b} \right)^2, \tag{8}$$

$$= \sum_m \sum_n \left(\frac{1}{a \cdot R_{blur}(m,n) + b} - \frac{1}{a \cdot R_0 + b} + \sum_{i=1}^{N} \frac{1}{k_i \cdot S_i(m,n)} \right)^2, \tag{9}$$

where m and n are the 2D spatial index.

To optimize the set of modeled parameters with respect to Φ, we perform an inversion using the *lsqnonlin* MATLAB function, which is based on a trust-region-reflective algorithm (Coleman and Li, 1994, 1996). It is an iterative optimization method in a least-square sense,

which is designed to solve non-linear inverse problems locally in subspace trust-regions. Each iteration involves the approximate solution of a large linear system using the method of preconditioned conjugate gradients. With regards to our inverse problem, the main advantages of this algorithm are that it solves a large variety of non-linear problems including our study, and handles parameter sets with both constrained and unconstrained bounds.

In addition to the misfit Φ, we also consider the 2*D* correlation ρ between R_{blur} and R_{model} to *a posteriori* assess the quality of the solution:

$$\rho = \frac{\sum_m \sum_n (R_{model}(m,n) - \overline{R}_{inv})(R_{blur}(m,n) - \overline{R}_{blur})}{\sqrt{\left(\sum_m \sum_n (R_{model}(m,n) - \overline{R}_{inv})\right)\left(\sum_m \sum_n (R_{blur}(m,n) - \overline{R}_{blur})\right)}}, \quad (10)$$

where $\overline{R}_{inv}$ and $\overline{R}_{blur}$ are the averaged values. ρ is free to vary between -1 (perfect anti-correlation), 0 (no correlation) and 1 (perfect correlation).

4. Results and parametric study

4.1. Modeled rebound

The inversion was performed only in the parts of the outcrop that are dominated by lime mudstones to prevent the results form potential lithological control by marls (Fig. 7F). To a first order, the spatial distribution of R_{model} and R_{blur} are consistent, the correlation coefficient ρ being equal to 0.55 (Fig. 8). Most distinctive features, including large north westernmost *R* and small *R* at the top of the outcrop, are matched. This spatial correspondence is interpreted to mean that the spatial distribution of fracture type and Schmidt hammer rebound can be used to assess effective elasticity and fault stiffness at a mesoscopic scale (0.1–1 m).

However, second-order discrepancies exist between the inverted model and the data: (1) especially at the bottom of the cataclasite core of the secondary fault ($X \sim 15$ m, $Y \sim 0.5$ m) where $R_{blur} > R_{model}$, which may be due to a variability of block dimensions and cohesion in the cataclasite cores that would affect the effective elasticity; (2) the fault at the center of the outcrop ($X \sim 10$ m) has little effect on *R*, unlike the model, so that $R_{blur} > R_{model}$; and (3) other discrepancies occur at the left of this secondary fault ($X \sim 13$ m, $Y \sim 1.8$ m) and at the extreme right of the outcrop ($X \sim 18$ m, $Y \sim 0.5$ m), such that for both $R_{blur} > R_{model}$. We suggest that these discrepancies may be related to the presence of small, unmeasured sealed fractures, that were not sampled due to their size. Despite these discrepancies, these observations imply that the spatial distribution of fracture type and spacing significantly controls the effective elasticity of the studied outcrop.

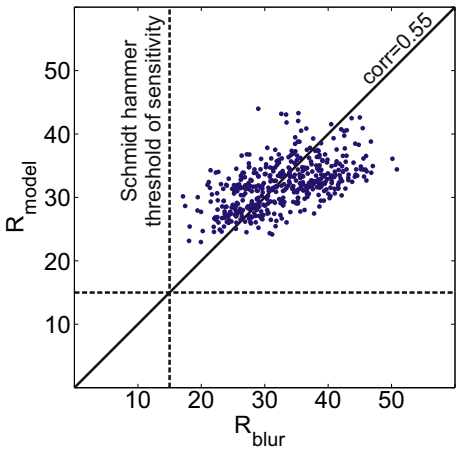

Fig. 8. Relationship between observed R_{blur} and inverted R_{model} Schmidt hammer rebound, with its associated coefficient of correlation. The threshold of sensitivity of the Schmidt hammer is indicated with a dashed line.

4.2. Optimal window size

Until now, we computed fracture spacing using a circular sliding window with a radius $L_{window} = 50$ cm. Still it is important to validate this choice and investigate the effect of varying L_{window} on the correlation coefficient ρ and misift Φ (Fig. 9A). ρ becomes greater than 50 for $L_{window} > 40$ cm, and reaches a maximum value, 0.63, for $L_{window} = 120$ cm, and then decreases. The misfit follows an inverse trend with the smallest misfit obtained for $L_{window} = 120$ cm.

These results constrain the sensitivity of the Schmidt hammer to rock mass volume: (1) the correlation coefficient is significant, $\rho > 0.5$ (Cohen, 1988), for $L_{window} > 40$ cm; (2) the Schmidt hammer reaches a maximum of sensitivity to the presence of fractures for a radius of $L_{window} = 120$ cm; and (3) the Schmidt hammer is sensitive to the presence of fracture beyond 2 m as ρ continues to exceed 0.5. Overall, these results validate the robustness of the inversion, as varying L_{window} to a small extent in the optimal window (40- $\sim$200 *cm*) does not dramatically change neither the correlation coefficient nor the misfit. This optimal window *aposteriori* gives support to the choice of $L_{window} = 50$ cm as the *apriori* window size to study the effect of fracture density with the Schmidt hammer.

4.3. Fracture type and R

Each fracture type has a different effect on *R* that can be quantified by inversion modeling. Indeed R_{model} is a combination of the contribution of each fracture type spacing (see Eq. (6)), weighted by their apparent stiffness. As we have no constraint for the values of apparent stiffnesses of the fractures, these parameters were set unbounded in the inversion. For $L_{window} = 50$ cm we have obtained the following set of apparent stiffnesses: $k_{fault} = 1.3 \cdot 10^{-1}$ GPa m^{-1}, $k_{open-fracture} = 8.9 \cdot 10^{-2}$ GPa m^{-1}, $k_{stylolite} = 1.8 \cdot 10^{-1}$ GPa m^{-1} and $k_{sealed-fracture} = 63.1$ GPa m^{-1}. Varying the radius of the sliding window does not significantly modify these values (Fig. 9B). Apparent stiffnesses remain approximatively constant for $L_{window} > 20$ cm. These results suggest that: (1) because faults, open fractures and stylolites exhibit small apparent stiffnesses, these fracture types generate most of the spatial variation for *R* on the outcrop; and (2) because sealed fractures have a large apparent stiffness, their contribution to *R* is negligible compared to other fracture types. Consequently, sealing or healing of fractures creates a dramatic increase of their stiffnesses.

4.4. Intact rock mass rebound

It is crucial to understand that these apparent stiffnesses are defined relatively to R_0 the intact rock or background rebound. Because R_0 reflects the rebound without any fractures, it cannot be measured at the outcrop. However, we assume that its value is greater than the maximum rebound of the outcrop, which is still for fracture rock. Thus, we have constrained the lower bound of this parameter in the inversion to 50. No constraint exist on the upper bound. Fig. 9C presents the variations of R_0 with L_{window}. For small or large value of L_{window}, R_0 is close to 60, whereas it is between 100 and 120 for L_{window} between 30 and 70 cm. The values obtained for R_0 are greater than 57.5 the maximum value of *R*, which is consistent with the physical meaning of R_0.

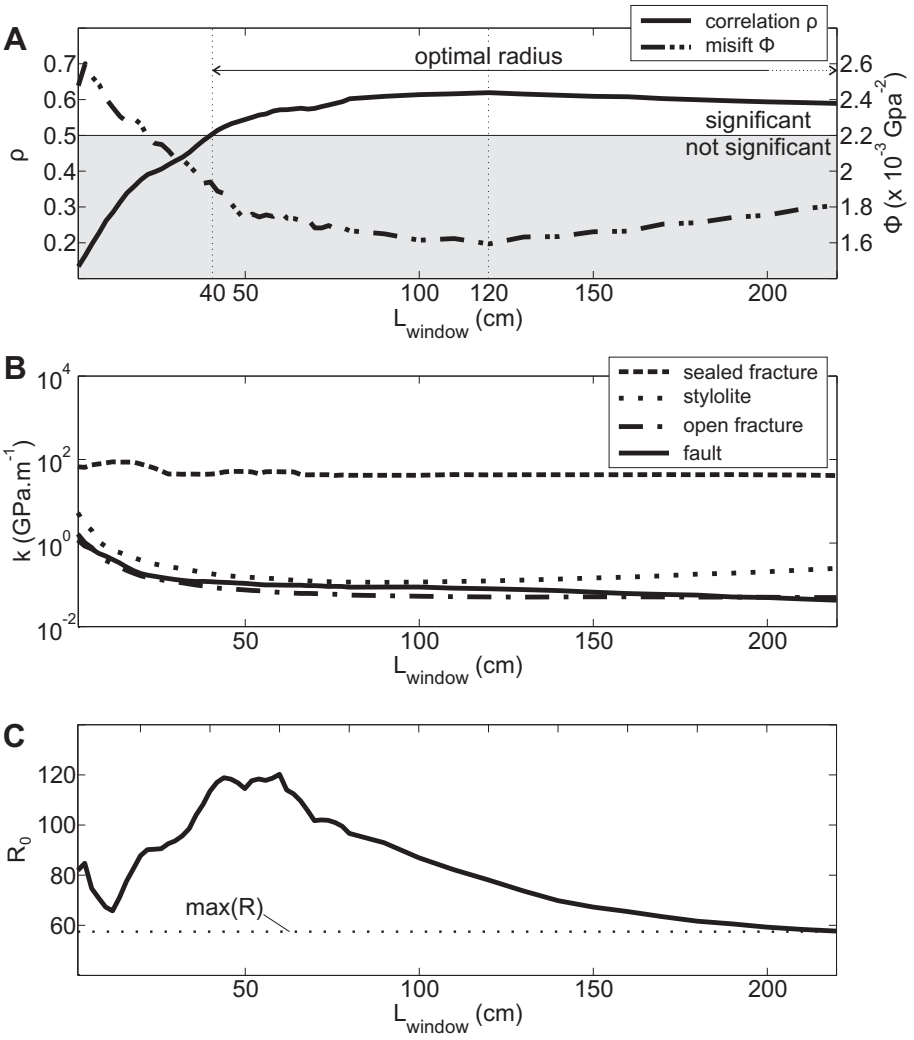

Fig. 9. Effect of the radius of the sliding window L_{window} used to compute fracture spacing on: (A) the correlation coefficient ρ (left) and misift Φ (right) between the observed R_{blur} and inverted R_{model} Schmidt hammer rebound; (B) the appparent stiffness for each fracture type infered from the non-linear least square inversion of R. The optimal window size zone is bounded by $L_{window} = 40$ cm where the correlation becomes significant and by $L_{window} \sim 200$ cm. (C) Evolution of the intact rock rebound R_0 with L_{window}. The maximum value of R is indicated by a dotted line.

4.5. Relationship between E and R

The results of the inversion also depend on the formalism and the parameterization of the relationship between the rebound R and Young's modulus E_{eff}. Following Sachpazis (1990), we used a linear relationship to perform the inversion, $E_{eff} = a \cdot R + b$. For carbonate laboratory rock samples, Sachpazis (1990) found that $a = 1.93$ and $b = -33.7$ best explain its dataset. However, this set of parameter is definitely not universal as many authors propose other formalisms to relate R and E_{eff} (see Aydin and Basu (2005), Goudie (2006), or Yagiz (2009) for a review of these formalisms). Thus, instead of keeping these two parameters constant in the inversion, we limit their ranges of variation around the values found by Sachpazis (1990): $1.7 < a < 2.25$ and $-70 < b < 10$. The inversion systematically converges toward $a = 2.25$ and $b = 10$.

Changing the formalism of the relationship between R and E_{eff} to a power law, $E_{eff} = b \cdot R^a$, and inverting the model using the parameters found by Yagiz, (2009) $a \simeq 1.5$ and $b \simeq 0.1$, leads to a modeled rebound R_{model} similar in its distribution to applying the linear relationship but with a greater misfit. The intact rock rebound R_0 remains about the same range of variation (75–125) as well as the sealed fracture stiffness, while the stiffnesses of the faults, open fractures and stylolites are about one order of magnitude less $\sim 10^{-2}$ GPa m^{-1} than for the linear relationship. We did not perform any test using an exponential relationship between R and E_{eff}, as to our knowledge no studies have documented this relationship for carbonates.

4.6. Lithological control on R

The outcrop is dominated by lime mudstones, but also includes marls and cataclastites, which are mostly located into the secondary fault zones (see Fig. 2A). We tried to directly invert the mechanical model (Eq. (6)) using the rebound and fracture spacing maps for the entire outcrop, including marls, lime mudstones and cataclasites. The results were not conclusive with a misfit orders of magnitude greater than when considering only lime mudstone in the inversion. This mismatch in R is the result of the presence in the marl-dominated secondary fault zone of both small fault spacing and small R values. This joint effect forces the inversion to converge toward very small value of apparent fault stiffness $k_{fault} = 2.2 \cdot 10^{-2}$ GPa m^{-1}. Thus, the small R values in the marl-dominated secondary fault zone are not explained by the concordant presence of faults only, but also probably by a lithological control.

To ascertain the effect on R of the lithological change to marl from lime mudstone, we modeled the rebound for the entire outcrop, $R_{model-all}$, using the parameters determined for lime mudstone and compared the results to the aggregate R_{blur} values (Fig. 10). The match between the model prediction and R_{blur} values is good except for the marl-dominated secondary fault zone. There, $R_{model-all}$ is 20–30 greater than $R_{blur.}$ If taking $R_0 = 100$ obtained with lime mudstone as the reference rebound, this lithological control represents about 25% of the signal.

5. Discussion

5.1. Fracture stiffness and model limitations

Because distinguishing between the elastic contribution of a fracture and the host rock is difficult, stiffness of fractures remains a poorly documented parameter. The results of this study suggest that the stiffness of sealed fractures is 10^1–10^2 GPa m^{-1}, while the stiffness of faults, stylolites and open fractures is ~0.1 GPa m^{-1}. These values compare reasonably well with the stiffnesses ~10^1 GPa m^{-1} found by Griffith et al. (2009) using the same mechanical model (Duncan and Goodman, 1968; Amadei and Savage, 1993) and fracture tracelength. However, they are orders of magnitude smaller than the stiffnesses 10^2–10^4 GPa m^{-1} found by Hardin et al. (1987) and Lubbe and Worthington (2006) using seismic methods on fractures with a characteristic length of ~1 m (Fig. 11). Because fracture stiffness linearly increases with fracture length (*e.g.*, Worthington and Lubbe, 2007), stiffnesses obtained in this study with a Schmidt hammer are equivalent to stiffnesses of fracture with a length of 10^2 to 10^3 m, as determined by seismic methods (Worthington and Hudson, 2000).

This discrepancy can be explained by several limitations of the mechanical model of this study. (1) The effective elastic model defined by Duncan and Goodman (1968) and Amadei and Savage (1993) assumes that stress and strain are homogeneous at the scale of the studied rock mass. As previously mentioned, this condition is not respected as the Schmidt hammer produces a point load, which is likely to generate a radial gradient of stress and strain centered on the impact point (Fig. 6). (2) In addition, the actual spatial distribution of fractures is not strictly uniform as compared to the models of Duncan and Goodman (1968) and Amadei and Savage (1993). (3) Also, we assumed that the contribution to deformability of each fracture set can be considered simultaneously, irrespective of potential mechanical interactions members of the different fracture sets.

In addition, it is important to note that both the Schmidt hammer and seismic methods suffer from common limitations: (1) because different subsets of fracture aperture are sampled by different elastic wave frequencies, fracture stiffness estimate is dependent on the frequency of the elastic waves generated by both methods (Pyrak-Nolte et al., 1990; Pyrak-Nolte and Nolte, 1992; Worthington and Lubbe, 2007); and (2) in-situ fracture stiffness estimates are dependent on the stress field, which controls the closure and the contact area of fractures (*e.g.*, Hillis, 1998; Jiang et al., 2009). These limitations prevent a robust and direct comparison of the absolute value of fracture stiffness obtained by the Schmidt hammer and by seismic methods in different tectonic settings. In that perspective, a comparative investigation of in-situ fracture stiffness obtained by both methods on a common outcrop is required. As a consequence, the relative stiffnesses of the different fracture sets obtained in this study is a more robust result than their absolute values.

5.2. Implications for fault zone rheology

Despite these limitations, our study represents a new insight into fault zone rheology. Fractures, such as sealed fractures, are located in the damage zone of faults (Caine et al., 1996; Gratier and Gueydan, 2007). Faults and fractures are created during seismic rupture, while sealed fractures result from sealing that occurs during the interseismic phase (*e.g.*, Sibson, 1992; Gratier et al., 1994; Renard et al., 2000; Gratier and Gueydan, 2007). Fracture sealing is the consequence of external material precipitation or deposition in the related veins (Gratier et al., 1994; Evans and Chester, 1995; Renard et al., 2000). It is likely to occur after previous pressure solution of the same material in stylolites (Gratier et al., 1994; Renard et al., 2000). According to experiments, the time scale of such fractures sealing, controlled by the kinetics of pressure

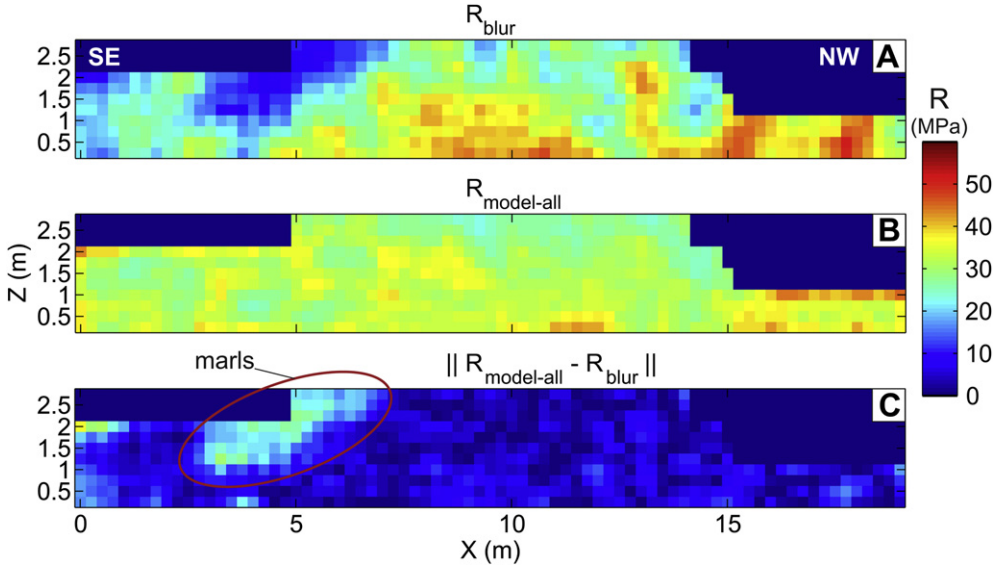

Fig. 10. Same as Fig. 7F, except that the set of model parameters inferred for the lime mudstones were used to extrapolate the modeled map to the entire outcrop: (A) observed $R_{blur.}$ (B) inverted $R_{model-all}$ Schmidt hammer rebound, and (C) difference between both along the entire study outcrop for $L_{window} = 50$ cm. The marly core zone of a secondary fault is indicated by a red circle. (For interpretation of the references to colour in this figure legend, the reader is referred to the web version of this article.)

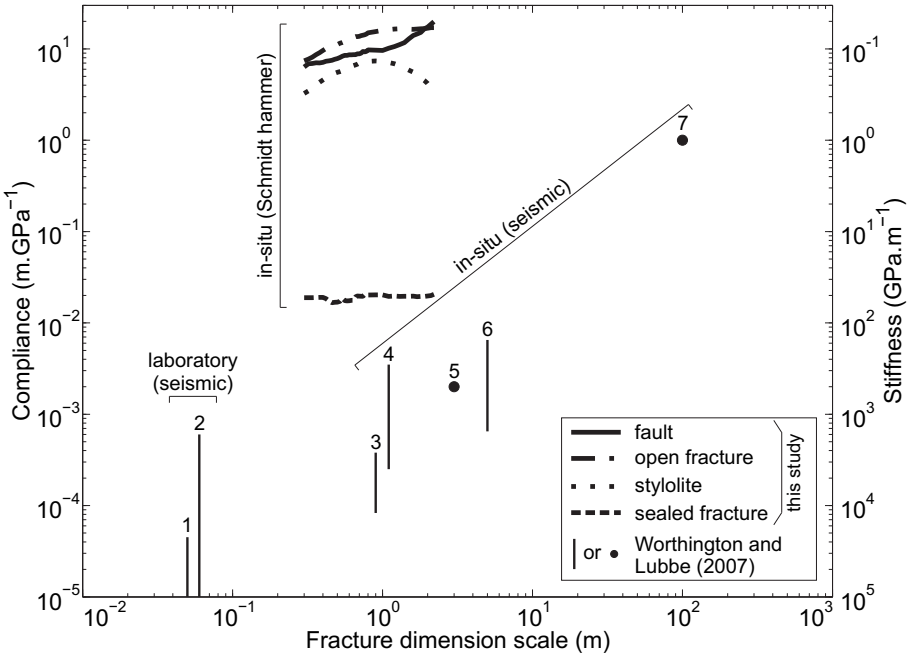

Fig. 11. Relationship between fracture compliance (inverse of stiffness) with the fracture dimension scale (modified from Worthington and Lubbe (2007)) for different methods of measurements. The four bold lines present the results of this study obtained in-situ with a Schmidt hammer in the range of the optimal window $40 < L_{window} < 120$ cm. Black vertical thin lines and black dots indicate the results of Worthington and Lubbe (2007), which compiled fracture stiffnesses from seismic laboratory experiments (1) Lubbe (2005), (2) Pyrak-Nolte et al. (1990) and seismic in-situ experiments (3) Hardin et al. (1987), (4) Lubbe and Worthington (2006), (5) King et al. (1986), (6) Herwanger et al. (2004) and (7) Worthington and Hudson (2000).

solution and associated with deposition processes, is on the order of several tens of years to several millions years, and is strongly dependent on temperature, fluid circulation, and rock texture (Rutter, 1976; Hickman and Evans, 1991; Gratier, 1993; Renard et al., 2000; Gratier and Gueydan, 2007).

Our results demonstrate that fracture sealing (or healing) increases fracture stiffness and the effective elasticity of the host rock, at least in carbonate rocks. Therefore, our results strongly support the interpretation that the seismically observed post-seismic increases in effective elasticity of the fault zones associated with Landers and Hector Mine earthquakes are due to fracture sealing (Li and Vidale, 2001; Li et al., 2003). More generally, our results support the assumption that the long-term joint effect of fracturing, pressure-solution creep, and sealing is to restore the rheological properties of fault zones during the interseismic phase, which may have geodynamical effects (Gratier and Gueydan, 2007). In particular, fracture sealing could potentially affect the relationship between plate tectonics far-field motion, and the interseismic stress build-up of major faults, by modulating the effective elasticity of the damage zone. Our results are consistent with an increase of the rate of interseismic stress build-up with sealing of fractures in the damage zone.

6. Conclusion

We have investigated the effective elasticty of a fault zone dominated by lime mudstones and exhibiting fractures with a characteristic length of a few centimeters to a few meters, using both a high density of Schmidt hammer measurements and a detailed map of fracture geometry. A mechanical model derived from effective elastic medium theory (Duncan and Goodman, 1968; Amadei and Savage, 1993), linking fracture spacing S to R, is inverted using a non-linear optimization method (Coleman and Li, 1994, 1996). The best modeled rebound is inferred when considering that the Schmdit hammer documents a hemispherical volume with a radius between 40 and ~200 cm. At the scale of the outcrop, R is mainly controlled by the distribution of fracture spacing and type. In addition, a lithological control is established (Zahm and Hennings, 2009; Zahm et al., 2010), with a change to marl from lime mudstone decreasing R by ~25%.

The results of the inversion are consistent with documented relationship between R and Young's modulus (Sachpazis, 1990; Yagiz, 2009). As expected, the intact rock rebound R_0 is greater than the maximum R value of the outcrop. The apparent stiffness of fractures, stylolites and open fractures is of the order of 10^{-1} GPa m^{-1}, two to three orders of magnitude lower than the stiffness of sealed fractures 10^1–10^2 GPa m^{-1}. Thus, fracture healing dramatically decreases fracture stiffness. However, these stiffnesses are significantly greater than the stiffnesses deduced from seismic experiments (Hardin et al., 1987; Lubbe and Worthington, 2006; Worthington and Lubbe, 2007), which could income from incompatibilities between the mechanical model (Duncan and Goodman, 1968; Amadei and Savage, 1993) and the settings of this study.

This study is the first attempt to constrain in-situ the relationships between fracture spacing and the effective elasticity of a rock mass using a Schmidt hammer. Our results may have geodynamical consequences, related for instance, to the interseismic stress build-up of major faults by sealing of fractures in the damage zone.

Acknowledgments

We gratefully thank Christopher K. Zahm, an anonymous reviewer, and William M. Dunne, for their careful reviews and suggestions which have considerably contributed to improve this manuscript. We thank Emmanuel David for fruitful discussions about effective elastic models, Dimitri Lague for helping with acquiring the geometry of the fracture networks from the field, and

also Benoît Gibert, Didier Loggia, Jérôme Lavé, Cédric Thieulot, Thomas Theunissen and Magali Rizza for helpful discussions. This study was funded by the Geosciences Montpellier laboratory research program ERODROCK.

References

Amadei, B., Savage, S.M., 1993. Effect of joints on rock mass strength and deformability. In: Brown, E.T., Hudson, J.A. (Eds.), Comprehensive Rock Engineering, vol. 1, pp. 331–365.

Arthaud, F., Mattauer, M., 1969. Sur les Décrochements NE-SW sénestres contemporains des plis pyrénéens du Languedoc. In: Extrait du, C.R. (Ed.), sommaire des séances de la Société Géologique de France, vol. 8, pp. 290–291.

Auzende, J.M., Bonnin, J., Olivet, J.L., 1973. The origin of the Western Mediterranean basin. Journal of the Geological Society, London 129, 607–620.

Aydin, A., Basu, A., 2005. The Schmidt hammer in rock material characterization. Engineering Geology 81, 1–14.

Aydin, A., 2009. ISRM Suggested method for determination of the Schmidt hammer rebound hardness: Revised version. International Journal of Rocks Mechanics Mining Science 46, 627–634.

Basu, A., Aydin, A., 2004. A method for the normalization of Schmidt hammer rebound values. International Journal of Rocks Mechanics Mining Science 41, 1211–1214.

Benedicto, A., 1996, Modèles tectono-sédimentaires de bassins en extension et style structural de la marge passive du Golfe du Lion (SE France), Thè de Doctorat, Université de Montpellier.

Ben-Zion, Y., Peng, Z., Okaya, D., Seeber, L., Armbruster, J.G., Ozer, N., Michael, A.J., Baris, S., Aktar, M., 2003. A shallow fault zone structure illuminated by trapped waves in the Karadere-Duzce branch of the North Anatolian Fault, western Turkey. Geophysical Journal International 152, 699–717.

Bieniawski, Z.T., 1978. Determining rock mass deformability: experience from case histories. Journal of Rock Mechanics and Mining Science and Geomech Abstracts 15, 237–248.

Bieniawski, Z.T., 1993. Classification of rock masses for engineering: the RMR system and future. In: Hoek, J.A., Hudson, J.A. (Eds.), Comprehensive Rock Engineering, vol. 3, pp. 553–573.

Belytschko, T., Plesha, M.E., Dowding, C.H., 1984. A computer method for stability analysis of caverns in jointed rock. International Journal Numerical and Analitical Methods Geomechanics 8, 473–492.

Bonnet, E., Bour, O., Odling, N.E., Davy, P., Main, I., Cowie, P., Berkowitz, B., 2001. Scaling of fracture systems in geologica media. Reviews of Geophysics 39, 347–383.

Bristow, J.R., 1960. Microcracks, and the static and dynamic elastic constants of annealed and heavily cold-worked metals. British Journal of Applied Physics 11, 81–85.

Bürgmann, R., Pollard, D.D., Martel, S.J., 1994. Slip distributions on faults: effects of stress gradients, inelastic deformation, heterogeneous host-rock stiffness, and fault interaction. Journal of Structural Geology 16 (12), 1675–1690.

Caine, J.S., Evans, J.P., Forster, C.B., 1996. Fault zone architecture and permeability structure. Geology 24, 1025–1028.

Cohen, J., 1988. Statistical Power Analysis for the Behavioral Sciences, second edition. Lawrence Erlbaum Associates, New Jersey.

Coleman, T.F., Li, Y., 1994. On the convergence of reflective Newton methods for large-scale nonlinear minimization subject to bounds. Mathematical Programming 76 (2), 189–224.

Coleman, T.F., Li, Y., 1996. An interior, trust region approach for nonlinear minimization subject to bounds. SIAM Journal on Optimization 6, 418–445.

Cowie, P.A., Scholz, C.H., 1992. Physical explanation for the displacement-length relationship of faults using a post-yield fracture mechanics model. Journal of Structural Geology 14 (10), 1133–1148.

Dearman, W.R., Baynes, J.F., Irfan, T.Y., 1978. Engineering grading of weathered granite. Engineering Geology 12, 345–374.

Deere, D.U., Miller, R.P., 1966. Engineering Classification and Index Properties for Intact Rock. Air Force Weapons Laboratory. technical report no. AFWL-TR 65–116, (Kirtland Base, New Mexico).

Duncan, J.M., Goodman, R.E., 1968. Finite element analyses of slopes in jointed rock in Final Report to U.S. Army Corps of Engineers, Vicksburg, MS, Report S-68–73.

Etchecopar, A., Vasseur, G., Daignieres, M., 1981. An inverse problem in microtectonics for the determination of stress tensors from faults striation analysis. Journal of Structural Geology 3, 51–65.

Evans, J.P., Chester, F.M., 1995. Fluid–rock interaction in faults of the San Andreas system: Inferences from San Gabriel fault rock geochemistery and microstructures. Journal of Geophysical Research 100, 13007–13020.

Fialko, Y., 2004. Probing the mechanical properties of seismically active crust with space geodesy: study of the co-seismic deformation due to the 1992 Mw7.3 Landers (southern California) earthquake. Journal of Geophysical Research 109 (B3), B03307.

Goudie, A.S., 2006. The Schmidt hammer in geomorphological research. Progress in Physical Geography 30, 703–718.

Gratier, J.P., 1993. Experimental pressure solution of halite by an indenter technique. Geophysical Research Letters 20, 1647–1650.

Gratier, J.P., Chen, T., Hellman, R., 1994. Pressure Solution as a Mechanism for Crack Sealing Around Faults, Proceedings of Workshop LXII on the Mecahnical involvment of fluids in faulting, 94-228, USGS open-file report, Menlo Par, pp. 279–300.

Gratier, J.P., Gueydan, F., 2007. Effect of fracturing and fluid-rock interaction on seismic Cycles. In: Handy, M.R., Hirth, G., Hovius, N. (Eds.), Tectonic Faults: Agents of Change on a Dynamic Earth, vol. 95, pp. 319–356.

Grechka, V., Kachanov, M., 2006. Effective elasticity of fractured rocks: a snapshot of the work in progress. Geophysics 71, W45–W58.

Griffith, W.A., Sanz, P.F., Pollard, D.D., 2009. Influence of outcrop scale fractures on the effective stiffness of fault damage zone rocks. Pure and Applied Geophysics 166, 1595–1627.

Guéguen, Y., Ravalec, M.L., Ricard, L., 2006. Upscaling: effective medium theory, numerical methods and the fractal dream. Pure and Applied Geophysics 163, 1175–1192.

Hardin, E.L., Cheng, C.H., Paillet, F.L., Mendelson, J.D., 1987. Fracture characterization by means of attenuation and generation of tube waves in fractured crystalline rock at Mirror Lake, New Hampshire. Journal of Geophysical Research 92, 7989–8006.

Herwanger, J.V., Worthington, M.H., Lubbe, R., Binley, A., Khazanehdari, J., 2004. A comparison of crosshole electrical and seismic data in fractured rock. Geophysical Prospecting 52, 109–121.

Hickman, S.H., Evans, B., 1991. Experimental pressure solution in halite – The effect of grain size interphase boundary structure. Journal of the Geological Society of London 148, 549–560.

Hillis, R.R., 1998. The influence of fracture stiffness and the in situ stress field on the closure of natural fractures. Petroleum Geoscience 4, 57–65.

Hudson, J.A., 1980. Overall properties of cracked solid. Mathematical Proceedings of the Cambridge Philosophical Society 88, 371–384.

Hudson, J.A., 1981. Wave speeds and attenuation of elastic waves in material containing cracks. Geophysical Journal of the Royal Astronomical Society 64, 133–150.

Jaeger, J.C., Cook, N.G.W., Zimmerman, R.W., 2007. Fundamentals of Rock Mechanics, fourth edition. Blackwell Publishing.

Jiang, X.W., Wan, L., Wang, X.S., Liang, S.H., Hu, B.X., 2009. Estimation of fracture normal stiffness using a transmissivity-depth correlation. International Journal of Rock Mechanics and Mining Sciences 46 (1), 51–58.

Kachanov, M., 1980. Continuum model of medium with cracks, Journal of the engineering mechanics Division. American Society of Civil Engineers 106, 1039–1051.

Kachanov, M., 1992. Effective elastic properties of cracked solids: Critical review of some basic concept. Applied Mechanics Review 45, 304–335.

Katz, O., Reches, Z., Roegiers, J.C., 2000. Evaluation of mechanical rock properties using a Schmidt hammer. International Journal of Rock Mechanics and Mining Sciences 37 (4), 723–728.

Kemeny, J., Cook, N.G.W., 1992. Effective moduli, non-linear deformation and strength of a cracked solid. Int. J. Rock Mech. Min. Sci. Geomech. Abstr. 23, 107–118.

King, M.S., Myer, L.R., Rezowalli, J.J., 1986. Experimental studies of elastic wave propagation in a columnar-jointed rock mass. Geophysical Prospecting 34, 1185–1199.

Li, Y.G., Vidale, J.E., 2001. Healing of the shallow fault zone from 19941998 after the 1992 M 7.5 Landers, California, earthquake. Geophysical Research Letters 28, 2999–3002.

Li, Y.G., Vidale, J.E., Day, S.M., Oglesby, D.D., Cochran, E., 2003. Postseismic fault healing on the rupture zone of the 1999 M 7.1 Hector Mine, California, earthquake. Bulletin of the Seismological Society of America 93, 854–869.

Lubbe, R., 2005, A field and laboratory investigation of the compliance of fractured rock, DPhil thesis, Oxford University.

Lubbe, R., Worthington, M.H., 2006. A field investigation of fracture compliance. Geophysical Prospecting 54, 319–332.

Mahtab, M. A., 1969, Three-dimensional finite element analysis of joint and rock slopes, Ph.D. thesis, Univ. of California, Berkeley.

McCarroll, D., 1991. The Schmidt hammer, weathering and rock surface roughness. Earth Surface Processes and Landforms 16, 477–480.

Molnar, P., Anderson, R.S., Anderson, S.P., 2007. Tectonics, fracturing of rock, and erosion. Journal of Geophysical Research 112 (F3), F030014.

Niedzielski, T., Migon, P., Placek, A., 2009. A minimum sample size required from Schmidt hammer measurements. Earth Surface Process and Landforms 34, 1713–1725.

O'Connell, R.J., Budiansky, B., 1974. Seismic velocities in dry and saturated cracked solids. Journal of Geophysical Research 79, 5412–5426.

Pyrak-Nolte, L.J., Myer, L.R., Cook, N.G.W., 1990. Transmission of seismic waves across single natural fractures. Journal of Geophysical Research 95, 8617–8638.

Pyrak-Nolte, L.J., Nolte, D.D., 1992. Frequency dependence of fracture stiffness. Geophysical Research Letters 19, 325–328.

Renard, F., Gratier, J.P., Jamtveit, B., 2000. Kinetics of crack-sealing, intergranular pressure solution, and compaction around active faults. Journal of Structural Geology 22, 1395–1407.

Renshaw, C.E., 1996. Mechanical controls on the spatial density of opening-mode fracture networks. Geology 25, 923–926.

Rispoli, R., 1981. Stress fields about strike-slip faults inferred from stylolites and tension gashes. Tectonophysics 75, T29–T36.

Rotonda, T., 2001. Applications of dynamic techniques to concrete lining of tunnels. In: Särkkä, P., Eloranta, P. (Eds.), Rock Mechanics: a Challenge for Society, pp. 603–608.

Rutter, E., 1976. The kinetics of rock–deformation by pressure solution. Philosophical Transactions of the Royal Society of London 283, 203–219.

Sachpazis, C.I., 1990. Correlating Schmidt hammer hardness with compressive strength and Young's modulus of carbonate rocks. Bulletin of Engineering Geology and Environment 42 (1), 75–93.
Sayers, C.M., Kachanov, M., 1995. Microcrack-induced elastic wave anisotropy of brittle rocks. Journal of Geophysical Research 100 (B3), 4149–4156.
Schlische, R.W., Young, S.S., Ackermann, R.V., Gupta, A., 1996. Geometry and scaling relations of a population of very small rifted related normal faults. Geology 24, 683–686.
Schoenberg, M., 1980. Elastic wave behavior across linear slip interfaces. The Journal of the Accoustical Society of America 68, 1516–1521.
Scholz, C.H., Cowie, P.A., 1990. Determination of geologic strain from fault slip data. Nature 346, 837–839.
Schultz, R.A., 2003. A method to relate initial elastic stress to fault population strain. Geophysical Research Letters 30, 1593.
Segall, P., Pollard, D.D., 1980. Mechanics of discontinuous faults. Journal of Geophysical Research 85 (B8), 4337–4350.
Séranne, M., Benedicto, A., Labaume, P., Truffert, C., Pascal, G., 1995. Structural style and evolution of the Gulf of Lion Oligo-Miocene rifting: role of the Pyrenean orogeny. Marine and Petroleum Geology 12 (8), 809–816.
Sibson, R.H., 1992. Implications of fault-valve behaviour for rupture nucleation and reccurence. Tectonophysics 211, 283–293.
Soliva, R., Maerten, F., Petit, J.P., Auzias, V., 2010. Field evidences for the role of static friction on fracture orientation in extensional relays along strike-slip faults: comparison with photoelasticity and 3-D numerical modeling. Journal of Structural Geology 32 (11), 1721–1731.
Sumner, P., Nel, W., 2002. The effect of rock moisture on Schmidt hammer rebound: tests on rock samples from Marion Island and South Africa. Earth Surface Processes and Landforms 27, 1137–1142.
Taha, M., 1986, Apport de la microtectonique cassante au problème des trajectoires de contraintes et de leurs perturbations. Exemples du Nord de Montpellier, thèse d'État, université de Montpellier.
Walsh, J.B., 1965. The effect of cracks on the compressibility of rocks. Journal of Geophysical Research 70, 381–389.
Worthington, M.H., Hudson, J.A., 2000. Fault properties from seismic Q. Geophysical Journal International 143, 937–944.
Worthington, M.H., Lubbe, R., 2007. The scaling of fracture compliance. Geol. Soc.Lond. Spec. Pub 207, 73–82.
Wu, H., Pollard, D.D., 1995. An experimental study of the relationship between joint spacing and layer thickness. Journal of Structural Geology 17, 887–905.
Xu, S., Grasso, P., Mahtab, A., 1990. Use of Schmidt Hammer for Estimating Mechanical Properties of Weak Rock. Proceedings of the 6th International IAEG Congress, 1. Balkema, Rotterdam, pp. 511–519.
Yagiz, S., 2009. Predicting uniaxial compressive strength, modulus of elasticity and index properties of rocks using the Schmidt hammer. Bulletin of Engineering Geology and the Environment 68 (1), 55–63.
Yilmaz, I., Sendir, H., 2002. Correlation of Schmidt hardness with unconfined compressive strength and Young's modulus in gypsum from Sivas (Turkey). Engineering Geology 66, 211–219.
Zahm, C.K., Hennings, P.H., 2009. Complex fracture development related to stratigraphic architecture: challenges for structural deformation prediction, Tensleep Sandstone at the Alcova anticline, Wyoming. AAPG Bulletin 93 (11), 1427–1446.
Zahm, C.K., Zahm, L.C., Bellian, J.A., 2010. Integrated fracture prediction using sequence stratigraphy within a carbonate fault damage zone, Texas, USA. Journal of Structural Geology 32, 1363–1374.